Structure and star formation in disk galaxies I. Sample selection and near infrared imaging

J. H. Knapen[1,2], R. S. de Jong[3], S. Stedman[1] and D. M. Bramich[4]

[1] *University of Hertfordshire, Department of Physical Sciences, Hatfield, Herts AL10 9AB*
[2] *Isaac Newton Group of Telescopes, Apartado 321, E-38700 Santa Cruz de La Palma, Spain*
[3] *Space Telescope Science Institute, 3700 San Martin Drive, Baltimore, MD 21218, USA*
[4] *School of Physics and Astronomy, University of St. Andrews, Scotland KY16 9SS*

ABSTRACT

We present near-infrared imaging of a sample of 57 relatively large, Northern spiral galaxies with low inclination. After describing the selection criteria and some of the basic properties of the sample, we give a detailed description of the data collection and reduction procedures. The K_s $\lambda = 2.2\mu$m images cover most of the disk for all galaxies, with a field of view of at least 4.2 arcmin. The spatial resolution is better than an arcsec for most images. We fit bulge and exponential disk components to radial profiles of the light distribution. We then derive the basic parameters of these components, as well as the bulge/disk ratio, and explore correlations of these parameters with several galaxy parameters.

Key words: galaxies: spiral – galaxies: structure – infrared: galaxies

1 INTRODUCTION

Near-infrared (NIR) imaging of galaxies is a better tracer of the underlying stellar structure than optical imaging, for two reasons. Firstly, the effects of extinction by dust in the galaxy are much reduced (an order of magnitude from V to K), and secondly, the NIR emission is a better tracer of the older stellar populations, which contain most of the stellar mass. The combined effect of these two factors is that NIR emission is a more accurate tracer of the mass in galaxies. This is also why the fraction of galactic bars, mostly devoid of current star formation (SF), is higher as determined from NIR than from optical surveys ($\sim$70% versus $\sim$ 55%, e.g., Sellwood & Wilkinson 1993; Mulchaey & Regan 1997; Knapen, Shlosman & Peletier 2000; Eskridge et al. 2000).

The main technical problems in NIR imaging of spiral disks are the high background at 2.2 micron, and the relatively small size of NIR array detectors. Detectors with 1024×1024 pixels, such as the ones used for the present paper, have only been in use since about 1996, and many of the cameras built around such arrays have been constructed to exploit the higher spatial resolution in the NIR, and/or the possibilities of adaptive optics (e.g., KIR on the CFHT, Doyon et al. 1998; UFTI on UKIRT, Roche et al. 2002). So whereas optical surveys of galaxy disks have been performed for decades, resulting, among many other results, in galaxy catalogues such as the RC3 (de Vaucouleurs et al. 1991), NIR surveys covering the whole disk of nearby spiral galaxies are

only now starting to be published (e.g., 2MASS: Skrutskie et al. 1997, Jarrett et al. 2003; Seigar & James 1998a, 1998b; Moriondo et al. 1999; Möllenhoff & Heidt 2001; Eskridge et al. 2002; this paper). The NIR cameras we used for the presently described project have been designed as a compromise between sampling the best seeing conditions and a relatively wide field of view (INGRID on the 4.2 m William Herschel Telescope, Packham et al. 2003), or specifically for wide-field imaging (PISCES on the 2.3 m Bok telescope, McCarthy et al. 2001). The presently described survey offers several advantages over most of the other studies mentioned above, namely by offering a set of high-resolution (the median value for the FWHM seeing across our sample is 0.90 arcsec), well-sampled (pixel size 0.24 arcsec for all but 4 images), reasonably deep images of a representative sample of nearby, not highly inclined, Northern spiral galaxies.

Decomposition of galaxy light in bulge and disk components has received renewed attention in recent years (e.g., Andredakis, Peletier & Balcells 1995; Byun & Freeman 1995; de Jong 1996a; Graham 2001; Möllenhoff & Heidt 2001). One of the main reasons for this renewed attention stems from the realisation that not all spheroids have $R^{\frac{1}{4}}$ de Vaucouleurs (1948) type profiles, but often are better fitted by $R^{\frac{1}{n}}$ Sersic (1968) type profiles. Furthermore, it has been suggested that the shape of the bulge and its relation to the disk may hold clues about the formation history of the galaxy components (e.g., Courteau, de Jong & Broeils 1996; Andredakis 1998; Graham 2001; Trujillo et al. 2002). It is now

generally believed that early-type spiral galaxies have bulges with de Vaucouleurs-like profiles (i.e. Sersic n values of order 4) and late-type spiral galaxies bulges with exponential-like profiles with $n \sim 1$, probably with a continuum in between. It has been suggested that the exponential bulges in late-type spiral galaxies are the result of bar instabilities driving gas toward the centre and scattering star in the vertical direction by buckling resonances, while the de Vaucouleurs type bulges are the result of accretion and merging events, probably early in the history of the galaxy (e.g., Courteau et al. 1996; Aguerri, Balcells & Peletier 2001). An alternative view was put forward by Andredakis et al. (1995), who proposed that the outer parts of $R^{\frac{1}{4}}$ bulges were strongly affected by the disk in late-type spiral galaxies, resulting in bulges with lower n values. Andredakis (1998) found that by growing a disk adiabatically on an existing $R^{\frac{1}{4}}$ bulge in a collisionless N-body simulation, he could indeed lower the n value of the resulting bulge, but not to values lower than $n = 2$.

In this paper, we present NIR imaging in the 2.2 micron K_s band of a complete sample of 57 nearby, not highly inclined, Northern spiral galaxies of all types. We also present fits to the separate bulge and disk components on the basis of radial surface brightness profiles. Optical broad (B, I) and narrow (Hα) band imaging of all galaxies in our sample will be presented in Paper II (Knapen et al. 2003). In Paper III (J. H. Knapen, in preparation) we study the morphology of the Hα emission in the central few kiloparsecs of the sample galaxies to explore the relative frequencies of, for instance, central peaks or nuclear rings among the sample. Correlations with morphological type or nuclear non-stellar activity will then be explored. In further papers, we will use ellipse fits to the NIR images to explore the parameters of the bars in the sample galaxies, and will use disk scale lengths to investigate whether, and in what fashion, these are affected by emission from young stars in areas of current star formation. The currently presented data set offers many more opportunities for study, and as examples we mention the study by Block et al. (2001) who derived gravitational torques due to bars from our NIR images, and the one by Jogee et al. (2002), who used one of our NIR images, of NGC 5248, to argue for the dynamical connection of the different components identified in that galaxy.

2   THE SAMPLE

2.1   Sample selection

Our sample of galaxies was selected from the list of Elmegreen and Elmegreen (1987), which contains 708 galaxies from the Second Reference Catalogue of Bright Galaxies (RC2; de Vaucouleurs et al. 1976). The Elmegreen and Elmegreen sample was selected to included all those galaxies listed in the RC2 with declination $\delta > -35°$, inclination $i < 60°$ and inclination-corrected diameter at 25 mag arcsec^{-2}, D_{25}, greater than 2 arcmin. Our sample of 57 galaxies was extracted from this large sample to give a smaller subset, primarily for analysis of the spiral arm properties, as follows:

- All galaxies of 4.2 arcmin and above in diameter (D_{25}) were selected to ensure that we could isolate the spiral arms, even at lower spatial resolutions.

- Galaxies with $\delta < -20°$ were excluded, ensuring all galaxies could be observed from the Northern hemisphere.
- Galaxies of inclination higher than $50°$, where we would have difficulty isolating the spiral structure, were excluded.

This gave a sample of 57 galaxies (Table 1) of which six have a diameter larger than 10 arcmin. The limitations of galaxy catalogues are various, due to their adopted criteria of inclusion and their degree of completeness. The RC2 from which the original sample was chosen is, as implied by its title, magnitude limited. No attempt has been made by us to investigate selection effects in the sample, but we note that the range of galaxies included in our sample is by nature limited in apparent diameter, brightness, and thus also in redshift z. This is a factor which must be taken into account with any conclusions drawn from the data.

Our sample of spiral galaxies covers the full range of morphological types from SA to SB, the full range of Hubble types, and the complete range of arm class from 1 to 12 (Elmegreen and Elmegreen 1987)[*]. The sample contains normal and active galaxies; isolated, companion and cluster member galaxies; disturbed and undisturbed galaxies; barred and un-barred galaxies; galaxies with and without extensive massive star forming regions; and galaxies with and without nuclear rings or other nuclear structure. Some of the most important of such basic parameters of the sample galaxies are given in Table 1. Stedman & Knapen (2001) present graphically the distribution of the sample galaxies as a function of morphological type, arm class, bar type, disk diameter, ellipticity, and systemic velocity, and we thus refer to the figures in that paper.

Of the sample galaxies, 23% are barred (RC3 type SB), 26% are un-barred (SA) and 51% are mixed (SX), giving a total of 74% of galaxies with bar structure. This is consistent with the findings of, e.g., Knapen et al. (2000), who estimate a bar fraction of approximately 2/3rds for all galaxies. Again based on classifications from the RC3, 25% of the sample galaxies possess an inner ring structure, 30% possess an inner s-shaped structure and 45% are mixed. The sample covers the full range of Hubble types from S0/a to Sm, with a marked excess of type bc and c galaxies. In fact, these two classes of open armed spirals contribute 40% of the total. Every arm class is represented in the sample, with 45% of the galaxies in classes 7, 8, 9 and 12, denoting grand design spiral arm structure. Our sample galaxies are fairly evenly distributed in recession velocity, lying mostly between 750 km s^{-1} and 1750 km s^{-1}, with a few galaxies at velocities between 2000 and 3000 km s^{-1}. We checked the NASA/IPAC Extragalactic Database (NED) for nuclear activity in our galaxies. As listed in Table 1, 27 galaxies (52%)

---

[*] Elmegreen & Elmegreen (1987) define arm classes as follows: arm class 1=chaotic, fragmented, unsymmetrical arms, 2=fragmented spiral arm pieces with no regular pattern, 3=fragmented arms uniformly distributed around the galactic centre, 4=only one prominent arm; otherwise fragmented arms, 5=two symmetric, short arms in the inner regions; irregular outer arms, 6=two symmetric inner arms; feathery ringlike outer structure, 7=two symmetric, long outer arms; feathery or irregular inner arms, 8=tightly wrapped ringlike arms, 9=two symmetric inner arms; multiple long and continuous outer arms, and 12=two long symmetric arms dominating the optical disk

are listed as showing some type of nuclear activity, of which almost half (13) are Seyferts and most others LINERs.

We conclude that although the sample is limited by its selection criteria, most importantly a lower limit on diameter and is therefore not "complete" in a strictly statistical sense, it is internally consistent and a fair, representative sample of all galaxies within the selection parameters, i.e., bright, relatively face-on spiral galaxies.

3 OBSERVATIONS AND DATA REDUCTION

3.1 INGRID observations

Images of all but four of our sample galaxies were obtained through the K_s filter with the INGRID NIR camera (Packham et al. 2003) at the Cassegrain focus of the 4.2 m William Herschel Telescope (WHT). The INGRID camera is built around a 1024×1024 pixel Hawaii detector array (HgCaTe), and gives a projected pixel size of 0.242 arcsec[†] with a field of view of 4.2 × 4.2 arcmin. Observations for this programme were made during a total of six allocated observing nights (May 14-16, 2000, Nov. 8 & 12, 2000 and Dec. 7, 2000), while additional images were collected during a number of service nights (Nov. 3, Dec. 4, 2000; March 9, Oct. 4, 2001; and Jan. 4, 2002). The image of NGC 3351 was obtained during the commissioning of INGRID, on the night of March 18, 2000. Conditions during most of the nights were good, photometric and with good seeing. Whereas for some galaxies images could only be obtained on one night, many were observed during different nights. The images of worst quality in terms of sky subtraction are of a number of galaxies around RA=14h, which could only be observed during our May 2000 nights, when the observations were hampered by clouds. Total exposure times range from 6 to 100 minutes on source, as listed in Table 2. Typical 1σ background noise is 20.5 mag arcsec^{-2}, depending on the observing time, down to 21.7 mag arcsec^{-2} for our longest exposure, of NGC 7741. This compares favourably with the value given for 2MASS images of bright galaxies, of 20.0 mag arcsec^{-2} (Jarrett et al. 2003).

The observing strategy consisted of small blocks of galaxy observations, each of some 5 minutes duration, interspersed with similar blocks of exposures of a nearby area of background sky, for an equal amount of time. The blocks consisted of 4 pointings, where in each pointing the galaxy centre was displaced by about 10 arcsec on the array. Each of these pointings in turn was built up from 3 to 5 individual exposures of 20 to 12 seconds, co-averaged to produce one FITS file after 60 second total exposure time. The high background in the K_s filter, variable and mostly dependent on the temperature of the outside air and the telescope, set the limit to the length of the individual exposures. The so-called dither pattern of 4 pointings serves to eliminate the bad pixels during the reduction, while the background sky exposures are paramount for sky subtraction (see below).

Whenever conditions were photometric, standard stars

[†] The pixel size of INGRID is 0.238 arcsec as of March 22nd, 2001. The few images we obtained after this date were re-gridded to the original pixel size of 0.242 arcsec.

from the list of Hawarden et al. (2001) were observed at regular intervals during the night.

3.2 INGRID data reduction

The data reduction was performed using a combination of standard and purpose-built IRAF and IDL tasks. The main reduction script has been adapted from a set of IDL procedures originally written by F. Rigaut and R. Doyon to reduce images taken with the KIR camera on the CFHT. The first step is the creation of a background frame from offset sky exposures taken before and after the galaxy frames. The different background frames are combined using an iterative median combination algorithm in order to remove stellar images and bad pixels which may be present in the individual exposures. In each of the (normally three) iterations the individual frames are compared with the median-combined frame produced from them, and any pixels which lead to peaks or troughs in the combined image of more than three times the noise are set to undefined in the offending single frame in the next iteration.

The background frame is then subtracted from each individual galaxy frame, and the background-subtracted galaxy frames are median-combined into the reduced image. In this latter step, bad pixels are masked out, and flatfielding is done on the individual frames. Since the galaxy is at a slightly different position in each individual frame, the position of either the nucleus of the galaxy or of a star in the field is determined and used to shift the images before combining them.

Where several images of the same galaxy were available, either taken during the same night or on different nights, these images were averaged after registering them using the positions of a number of foreground stars, and/or the nucleus of the galaxy. The procedures used for the alignment were very similar to those described in §3.4, below, for the registering of NIR and optical images. What we will refer to as "final" images are those which have been registered with the optical images of our data set (as described in detail in Paper II).

Photometric calibration was performed by comparison of the final, combined, images with the reduced images as obtained on individual photometric nights. For those nights, calibration constants were derived from the observations of photometric standard stars. We measured the total flux in the two images in a circular aperture centred on the nucleus of the galaxy, making sure that exactly the same area was taken for both the photometrically calibrated and the final image. Correcting for background and pixel size, which are in some cases different in the photometric and final images, we thus calibrate the final images.

3.3 PISCES observations and data reduction

Images of four of our sample galaxies were obtained using the PISCES camera on the Bok 2.3 m telescope of the Steward Observatory, on Oct. 17 (NGC 6946) and 18 (NGC 628, 1068, 6184), 1999. The PISCES camera (McCarthy et al. 2001) uses the same kind of array as INGRID, but gives pixels of 0.''5 on the sky. The details of the observations, data reduction and calibration procedures for these images

Galaxy		Type		Activity	D_{25}	Arm	i	PA	M_B	v	D	Scale
NGC	M	(RC3)	(Carnegie)	(NED)	(′)	Class	(°)	(°)		(km s^{-1})	(Mpc)	(pc/″)
0210		.SXS3	Sb		5	6	35	160	11.6	1634	20.3	98
0337A		.SXS8	Sc		5.9	2	28	10	12.7	1076	13.7	66
0488		.SAR3	Sab		5.3	3	30	15	11.15	2269	29.3	142
0628	74	.SAS5	Sc		10.5	9	16	25	9.95	656	9.7	47
0864		.SXT5	Sbc		4.7	5	28	20	11.4	1560	20.0	97
1042		.SXT6	Sc		4.7	9	27	15	11.56	1373	16.7	81
1068	77	RSAT3	Sb	Sy1 Sy2	7.1	3	22	70	9.61	1137	14.4	70
1073		.SBT5	SBc		4.9	5	16	15	11.47	1211	15.2	74
1169		.SXR3	Sba		4.2	3	34	28	12.2	2387	33.7	163
1179		.SXR6	SBc		4.9	3	27	35	12.6	1780	21.2	103
1300		.SBT4	SBb/SB0		6.2	12	35	106	11.11	1568	18.8	91
2775		.SAR2	Sa		4.3	3	27	155	11.03	1354	17.0	82
2805		.SXT7			6.3	5	28	125	11.52	1734	28.0	136
2985		PSAT2	Sab	LINER	4.6	3	26	0	11.18	1322	22.4	109
3184		.SXT6	Sc	HII	7.4	9	14	135	10.36	593	8.7	42
3227		.SXS1P	S0/Sb	Sy1.5	5.4	7	34	155	11.1	1157	20.6	100
3344		RSXR4	Sbc		7.1	9	16		10.45	586	6.1	30
3351	95	.SBR3	SBb	HII Sbrst	7.4	6	34	13	10.53	778	8.1	39
3368	96	.SXT2	Sab	Sy LINER	7.6	8	33	5	10.11	897	8.1	39
3486		.SXR5	Sbc	Sy2	7.1	9	30	80	11.05	682	7.4	36
3631		.SAS5	Sbc		5	9	11		11.01	1158	21.6	105
3726		.SXR5	Sbc		6.2	5	33	10	10.91	849	17.0	82
3810		.SAT5	Sc		4.3	2	32	15	11.35	994	16.9	82
4030		.SAS4			4.2	9	31	27	12.02	1460	25.9	126
4051		.SXT4	Sbc	Sy1.5	5.3	5	30	135	10.83	725	17.0	82
4123		.SBR5	SBbc	Sbrst HII	4.4	9	30	135	11.98	1329	25.3	123
4145		.SXT7	Sc	HII/LINER	5.9	4	31	100	11.78	1016	20.7	100
4151		PSXT2*	Sab	Sy1.5	6.3	5	32	50	11.5	995	20.3	98
4242		.SXS8	Sd/SBd		5	1	28	25	11.37	517	7.5	36
4254	99	.SAS5	Sc		5.4	9	20		10.44	2407	16.8	81
4303	61	.SXT4	Sc	HII Sy2	6.5	9	14		10.18	1569	15.2	74
4314		.SBT1	SBa	LINER	4.2	12	18		11.43	963	9.7	47
4321	100	.SXS4	Sc	LINER HII	7.4	12	22	30	10.05	1586	16.8	81
4395		.SAS9*	Sd/SBd	LINER Sy1.8	13.2	1	23	147	10.64	320	3.6	18
4450		.SAS2	Sab	LINER	5.3	12	30	175	10.9	1956	16.8	81
4487		.SXT6	Sc		4.2	5	34	100	12.26	1037	19.9	97
4535		.SXS5	SBc		7.1	9	32	0	10.59	1957	16.8	81
4548	91	.SBT3	SBb	LINER Sy	5.4	5	26	150	10.96	486	16.8	81
4579	58	.SXT3	Sab	LINER Sy1.9	5.9	9	26	95	10.48	1519	16.8	81
4618		.SBT9	SBbc	HII	4.2	4	24	25	11.22	544	7.3	35
4689		.SAT4	Sc		4.3	3	24		11.6	1619	16.8	81
4725		.SXR2P	SBb	Sy2	10.7	6	32	35	10.11	1206	12.4	60
4736	94	RSAR2	Sab	Sy2 LINER	11.2	3	24	105	8.99	310	4.3	21
5247		.SAS4	Sc		5.6	9	20	20	10.5	1357	22.2	108
5248		.SXT4	Sbc	Sy2 HII	6.2	12	31	110	10.97	1153	22.7	110
5334		.SBT5*	SBc		4.2	2	31	15	11.99	1382	24.7	120
5371		.SXT4	Sb/SBb	LINER	4.2	9	26	8	11.32	2553	37.8	183
5457	101	.SXT6	Sc		28.8	9	14		8.31	241	5.4	26
5474		.SAS6P	Scd/SBcd	HII	4.8	2	18		11.28	273	6.0	29
5850		.SBR3	SBb		4.3	8	20	140	11.54	2556	28.5	138
5921		.SBR4	SBbc	LINER	4.9	8	24	130	11.49	1480	25.2	122
5964		.SBT7			4.2	2	27	145	12.6	1447	24.7	120
6140		.SBS6P			6.3	2	31	95	11.81	910	18.6	90
6384		.SXR4	Sb	LINER	6.2	9	35	30	11.14	1663	26.6	129
6946		.SXT6	Sc	HII	11.5	9	22		9.61	52	5.5	27
7727		SXS1P	Sa		4.7	1	28	35	11.5	1814	23.3	113
7741		.SBS6	SBc		4.4	5	34	170	11.84	755	12.3	60

Table 1. Global parameters of the galaxies in the observed sample. Except where otherwise mentioned, all figures are from the RC3. Tabulated are NGC (column 1) and Messier numbers (column 2) of the sample galaxies; morphological type from the RC3 (column 3) and from the Carnegie Atlas of Galaxies (Sandage & Bedke 1994; column 4); nuclear activity from the NED (column 5); apparent major isophotal diameter measured at or reduced to surface brightness level $\mu_B = 25.0\,B$-mag arcsec^{-2}(D_{25}; column 6); Elmegreen arm class (from Elmegreen and Elmegreen 1987; column 7), where the arm class ranges from 1 (flocculent) to 12 (grand design); inclination (i; column 8), from the ratio of the major to the minor isophotal diameter; position angle PA of the major axis of the disk (column 9); total magnitude M_B (column 10); mean heliocentric radial velocity as derived from neutral hydrogen observations (v; column 11); distance from the Nearby Galaxies Catalog (Tully 1988; column 12) and image scale (column 13), as derived from the distance.

are described in McCarthy et al. (2001) and only the essentials are repeated here. The PISCES camera has an 8.5 arcmin circular field of view and the galaxies were mosaiced with a few central images and many overlapping images in the outer parts, interspaced with sky offset images. Flatfields were created by differencing a number of early and late twilight images. The flatfielded object images were sky subtracted by weight-averaged and clipped offset sky frames. The object images were corrected for image distortions and then optimally combined using cross-correlations for positional offsets and using airmass coefficient calibrations for intensity matching. Effective exposure times range typically from about 1000 s in the outer regions to 2000 s in the centre. Seeing on the combined images is 2.5 arcsec for the Oct. 17 observation and 1.5 arcsec for those of Oct. 18. Calibration was performed by observing standard star fields from the list of Hunt et al. (1998) at least 4 times a night at several airmasses, to allow accurate calculation of airmass and colour terms.

3.4 Final data sets

Since we are interested in comparing the NIR images with the optical images we have obtained for our sample galaxies, we have used a special procedure to make the NIR images directly comparable to the others. This procedure is described in detail in Paper II, where we also describe the optical observations and their reduction, but in outline the following was done. We determined the positions of three foreground stars (or failing that, two stars plus the galaxy nucleus) in each of the images to be combined, as well as in an astrometrically calibrated image which we obtained from the Digitized Sky Survey (DSS). From these positions, an IRAF script we developed calculates the translation, rotation, and scaling needed for each image. It also determines which image has the highest resolution (smallest pixels) and the largest extent. Finally, the rotation needed to place the image set in an RA, dec orientation is determined from the position of the stars in the DSS image. Images are then rotated, translated and scaled in such a way that the resulting images are correctly oriented, have the pixel size of the image with the smallest pixels, and the extend of that covering the largest area. Those images covering a smaller area are filled with zero-valued pixels. Even though the resulting images may contain many more pixels, and are thus much larger, this is the only way to ensure that no information is lost. Table 2 gives the size of the fully reduced K_s images, but before the operations described immediately above. The area given in the Table thus represents the useful size of the NIR images. Table 2 also lists with which telescope the images were obtained, as well as the total on-source exposure time and the spatial resolution. The NIR images of all galaxies are shown in Fig. 1.

4 BULGE/DISK DECOMPOSITION

In recent years, performing bulge/disk (B/D) decompositions in two dimensions, i.e., on the full image, instead of in one dimension, on the luminosity profiles, has become the accepted norm (e.g., Byun & Freeman 1995; de Jong 1996a; Möllenhoff & Heidt 2001; Simard et al. 2002; Tran et al.

Galaxy	Telescope	Exp. time (min)	Seeing (arcsec)	Size (arcmin)
NGC 0210	WHT	24	1.04	4.2
NGC 0337A	WHT	28	1.04	4.2
NGC 0488	WHT	45	1.68	4.9
NGC 0628	Bok	N/A	1.55	11.0
NGC 0864	WHT	24	0.94	4.2
NGC 1042	WHT	45	2.16	4.8
NGC 1068	Bok	N/A	1.64	9.6
NGC 1073	WHT	24	1.02	4.2
NGC 1169	WHT	24	0.78	4.2
NGC 1179	WHT	28	0.89	4.2
NGC 1300	WHT	32	1.03	5.2
NGC 2775	WHT	12	0.78	4.2
NGC 2805	WHT	48	1.06	4.2
NGC 2985	WHT	20	1.14	4.2
NGC 3184	WHT	24	0.89	5.1
NGC 3227	WHT	12	0.73	4.7
NGC 3344	WHT	24	0.85	4.9
NGC 3351	WHT	12	1.14	7.4
NGC 3368	WHT	8	0.77	5.0
NGC 3486	WHT	24	0.83	4.9
NGC 3631	WHT	38	0.87	4.2
NGC 3726	WHT	12	0.69	4.2
NGC 3810	WHT	12	0.69	4.2
NGC 4030	WHT	30	0.69	4.2
NGC 4051	WHT	12	0.74	4.8
NGC 4123	WHT	28	0.76	4.2
NGC 4145	WHT	36	1.04	4.2
NGC 4151	WHT	12	0.75	4.8
NGC 4242	WHT	24	1.26	4.2
NGC 4254	WHT	12	0.82	4.2
NGC 4303	WHT	19	1.06	4.8
NGC 4314	WHT	35	2.02	4.2
NGC 4321	WHT	12	0.76	5.0
NGC 4395	WHT	20	1.04	4.8
NGC 4450	WHT	12	0.89	4.7
NGC 4487	WHT	13	0.83	4.2
NGC 4535	WHT	12	0.77	5.0
NGC 4548	WHT	12	0.81	4.8
NGC 4579	WHT	12	0.98	4.8
NGC 4618	WHT	28	1.16	4.2
NGC 4689	WHT	12	0.81	4.2
NGC 4725	WHT	24	0.97	6.0
NGC 4736	WHT	19	0.98	5.2
NGC 5247	WHT	12	0.81	4.8
NGC 5248	WHT	12	0.79	4.8
NGC 5334	WHT	16	0.94	4.2
NGC 5371	WHT	12	0.91	4.2
NGC 5457	WHT	6	3.03	4.2
NGC 5474	WHT	16	1.00	4.2
NGC 5850	WHT	12	0.93	4.2
NGC 5921	WHT	12	1.02	4.2
NGC 5964	WHT	32	0.82	4.2
NGC 6140	Bok	N/A	1.74	8.0
NGC 6384	WHT	8	0.70	4.2
NGC 6946	Bok	N/A	2.31	11.6
NGC 7727	WHT	56	0.82	4.2
NGC 7741	WHT	75	0.90	4.8

Table 2. Properties of the final NIR images: telescope used to obtain the image (col. 2), total on-source exposure time in minutes (col. 3), seeing as measured from the final image (in arcsec; col. 4), and field of view on the final image (in arcmin, where images are assumed to be square; col. 5).

Figure 1. K_s images of all galaxies in the sample. North is up and East to the left in all images, and the scale of each individual image is indicated by the white bar in the bottom right corner, which represents a length of 1 arcmin. Indicative contours are shown at surface brightness levels of 17 and 15 mag arcsec^{-2} for all galaxies, *except* the following, for which contours are shown at 16 and 15 mag arcsec^{-2}: NGC 2775, NGC 3368, NGC 4030, NGC 4051, NGC 4254, NGC 4303, NGC 4535, NGC 4548, NGC 4736, NGC 5248, NGC 6384.

2003). We have made 2D fits to our K-band images using the GIM2D code (Simard et al. 2002). Unfortunately, due to limitations in the signal-to-noise ratio and image extent, and due to mosaicing imperfections, 2D fitting of our K-band images proved to be highly unstable. We therefore resorted to 1D B/D fitting, pointing out that at least the resulting disk parameters (and most of the bulge parameters) will be equal within the errors of the fit in the 1D and 2D cases (de Jong 1996a; MacArthur et al. 2003). In addition, for face-on galaxies 1D and 2D fitting is nearly identical when no non-axisymmetric features (bars, arms) are fitted and error weighting is done consistently.

We used the IRAF ellipse fitting tasks to fit radial profiles to the surface brightness distribution in all images. We used sets of fixed position angle ellipticity for each galaxy, as taken from the RC3 and checked with our NIR and optical (Paper II) images. The resulting azimuthally averaged profiles are shown in Fig. 2. The 1D fitting technique we used is very similar to the one described in de Jong (1996a), with some modifications reflecting the investigations described by MacArthur et al. (2003). The Levenberg-Marquardt nonlinear least-squares fitting technique was used. For the disks we used exponential profiles, for the bulges Sersic profiles. Before fitting, the model profiles were convolved with Gaussian seeing profiles with FWHMs equal to the FWHMs measured on foreground stars in the images. To reduce the effects of uncertainties in the seeing profiles, we discarded the inner few points, namely those with radii less than two tenths of the FWHM seeing value. Relative weights of the profile data points were set to reflect photon statistics, uncertainties due to sky measurement errors, seeing errors and errors due to unmodelled features. The latter correction is necessary because the light profiles contain features that are not modelled, like bars and spiral arms, which cause residuals in the fit (see e.g., de Jong 1996a, his fig. 3). Not taking the unmatched components into account will result in reduced χ^2 values much larger than 1. We have used an uncertainty of 0.05 mag rms at each data point due to unmatched components in our weighting scheme.

As shown by MacArthur et al. (2003), fitting Sersic profiles with a free n value is very unstable and often results in non-physical results. We have used a similar grid search technique as them, fitting the profiles with fixed Sersic n values, with n ranging from 0.5 to 5 in steps of 0.1. Unlike MacArthur et al. (2003), we did not use a combination of an inner and a global χ^2 to select the best fit, but used only the χ^2 of the whole profile fit to select the best fit.

All fits were repeated with the maximum sky error estimate added and subtracted from the luminosity profile. This provides a reliable estimate of the uncertainties in the bulge and disk parameters, as it has shown before that sky errors dominate B/D decompositions (e.g., de Jong 1996a; MacArthur et al. 2003). The fits of many galaxies had large errors because of the limited field of view of the detector compared to the galaxy size and the limits of mosaicing in the near-IR. We therefore decided to exclude all disk param-
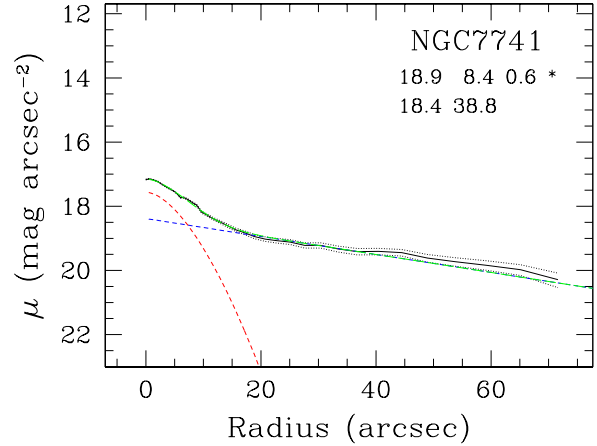

Figure 2. Continued.

eters if the uncertainty in their central surface brightness (μ_0) or disk scale length (h) was larger than 30% or if the fitted scale length was larger than half the image size. Likewise, bulge fits were rejected if the error in the effective radius ($R_{e,B}$) or in the surface brightness at this radius ($\mu_{e,B}$) was larger than 30%, if $R_{e,B}$ was smaller than the FWHM of the seeing, or if $n \leq 0.8$ (as is the case for NGC 3351 and NGC 7741 which have disturbed centres). This strict selection leaves only 13 of the 57 galaxies with both reliable disk and bulge parameters. In Fig. 2 we show the fits for all those galaxies where either bulge or disk fit was reliable.

Fitting results for those galaxies with at least a reliable bulge or a reliable disk fit are presented in Fig. 3 and Table 3. Fits are not plotted for those galaxies where both bulge and disk parameters could not reliably be determined. Bulge or disk parameters that were poorly determined are marked by a star in Fig. 2.

In what follows, photometric parameters were corrected for Galactic foreground extinction following the precepts of Schlegel, Finkbeiner & Davis (1998). Distances to put measurements at an absolute scale were obtained from the Nearby Galaxies Catalog (Tully 1988). Disk surface brightnesses were corrected to face-on values using the fully transparent correction of $\mu_0^i = \mu_0 - 2.5 \log(1 - \epsilon)$, where the ellipticities ϵ were taken from the RC3 but double-checked with the outer parts of the images.

Many combinations between the various bulge and disk parameters can be investigated, but with so few reliable decompositions we refer to previous work for most of them

Name	$\mu_{e,B}$ (mag arcsec^{-2})	$R_{e,B}$ (arcsec)	n	μ_0 (mag arcsec^{-2})	h (arcsec)
NGC 0337A	$21.08^{+0.08}_{-0.08}$	$25.73^{+5.49}_{-7.42}$	$0.9^{+0.1}_{-0.1}$	$19.79^{+0.30}_{-0.32}$	$65.40^{+20.32}_{-38.61}$
NGC 0488	$16.35^{+0.13}_{-0.37}$	$9.20^{+0.87}_{-2.65}$	$1.8^{+0.1}_{-0.3}$	$16.64^{+0.15}_{-0.30}$	$34.18^{+3.81}_{-7.40}$
NGC 0628	$18.24^{+0.03}_{-0.14}$	$22.44^{+0.80}_{-3.20}$	$1.5^{+0.1}_{-0.1}$	$17.68^{+0.05}_{-0.12}$	$82.42^{+5.86}_{-9.40}$
NGC 0864	$18.36^{+0.34}_{-1.09}$	$6.81^{+1.37}_{-6.74}$	$3.0^{+0.3}_{-1.0}$	$17.47^{+0.09}_{-0.18}$	$31.86^{+3.20}_{-5.22}$
NGC 1042	$18.64^{+0.21}_{-0.40}$	$6.42^{+0.78}_{-1.73}$	$2.1^{+0.2}_{-0.4}$	$18.69^{+0.07}_{-0.23}$	$49.40^{+6.88}_{-9.23}$
NGC 1169	$16.42^{+0.12}_{-0.13}$	$7.22^{+0.59}_{-0.71}$	$1.6^{+0.1}_{-0.1}$	$16.81^{+0.10}_{-0.12}$	$33.49^{+2.97}_{-3.68}$
NGC 1179	$19.31^{+0.07}_{-0.14}$	$5.54^{+0.34}_{-0.68}$	$1.7^{+0.1}_{-0.1}$	$18.92^{+0.04}_{-0.08}$	$31.57^{+2.33}_{-5.01}$
NGC 1300	$16.56^{+0.03}_{-0.11}$	$7.24^{+0.17}_{-0.48}$	$1.9^{+0.1}_{-0.1}$	$18.05^{+0.06}_{-0.10}$	$48.71^{+2.39}_{-9.73}$
NGC 2775	$16.34^{+0.26}_{-0.28}$	$9.27^{+1.55}_{-2.12}$	$2.4^{+0.2}_{-0.2}$	$15.95^{+0.15}_{-0.19}$	$26.20^{+2.28}_{-3.17}$
NGC 3227	$14.36^{+0.11}_{-0.20}$	$2.86^{+0.16}_{-0.32}$	$1.9^{+0.1}_{-0.2}$	$16.27^{+0.12}_{-0.17}$	$25.64^{+3.11}_{-4.74}$
NGC 3351	$15.45^{+0.03}_{-0.03}$	$9.46^{+0.18}_{-0.18}$	$0.8^{+0.1}_{-0.1}$	$16.58^{+0.06}_{-0.05}$	$45.44^{+5.30}_{-5.48}$
NGC 3631	$17.21^{+0.11}_{-0.03}$	$10.30^{+0.69}_{-0.27}$	$1.8^{+0.1}_{-0.1}$	$18.65^{+0.16}_{-0.08}$	$64.58^{+7.11}_{-5.32}$
NGC 3810	$16.15^{+0.25}_{-0.13}$	$3.43^{+0.59}_{-0.37}$	$1.5^{+0.2}_{-0.1}$	$15.68^{+0.12}_{-0.06}$	$15.96^{+1.70}_{-0.91}$
NGC 4051	$14.85^{+0.18}_{-0.19}$	$3.22^{+0.29}_{-0.34}$	$2.5^{+0.2}_{-0.2}$	$17.24^{+0.15}_{-0.14}$	$48.23^{+11.97}_{-17.52}$
NGC 4303	$15.03^{+0.09}_{-0.03}$	$4.46^{+0.19}_{-0.09}$	$1.3^{+0.1}_{-0.1}$	$16.51^{+0.06}_{-0.04}$	$39.54^{+3.72}_{-3.68}$
NGC 4535	$16.19^{+0.21}_{-0.11}$	$3.98^{+0.42}_{-0.27}$	$2.1^{+0.2}_{-0.1}$	$17.57^{+0.07}_{-0.04}$	$63.45^{+11.07}_{-11.28}$
NGC 4689	$19.10^{+0.14}_{-0.31}$	$14.79^{+1.83}_{-5.07}$	$2.1^{+0.1}_{-0.2}$	$17.78^{+0.07}_{-0.18}$	$42.95^{+5.58}_{-11.15}$
NGC 4725	$16.46^{+0.13}_{-0.13}$	$16.16^{+1.35}_{-1.55}$	$2.5^{+0.1}_{-0.1}$	$17.30^{+0.14}_{-0.14}$	$83.67^{+15.25}_{-21.72}$
NGC 5247	$18.88^{+0.05}_{-0.15}$	$23.38^{+1.58}_{-3.03}$	$2.3^{+0.1}_{-0.1}$	$18.22^{+0.13}_{-0.30}$	$90.97^{+16.96}_{-31.96}$
NGC 5371	$16.20^{+0.03}_{-0.03}$	$6.06^{+0.17}_{-0.17}$	$1.8^{+0.1}_{-0.1}$	$17.14^{+0.05}_{-0.10}$	$51.44^{+6.52}_{-10.73}$
NGC 5457	$18.63^{+0.14}_{-0.06}$	$21.82^{+2.23}_{-1.64}$	$2.1^{+0.1}_{-0.1}$	$17.50^{+0.06}_{-0.06}$	$128.07^{+17.13}_{-14.97}$
NGC 5474	$19.46^{+0.03}_{-0.03}$	$18.16^{+0.75}_{-0.75}$	$0.9^{+0.1}_{-0.1}$	$19.71^{+0.13}_{-0.13}$	$81.29^{+24.87}_{-30.05}$
NGC 5850	$17.50^{+0.14}_{-0.25}$	$14.05^{+1.46}_{-2.68}$	$2.9^{+0.1}_{-0.2}$	$18.25^{+0.33}_{-0.41}$	$39.11^{+10.05}_{-19.20}$
NGC 5921	$15.54^{+0.12}_{-0.22}$	$3.59^{+0.27}_{-0.26}$	$1.6^{+0.1}_{-0.1}$	$17.37^{+0.23}_{-0.26}$	$30.43^{+10.74}_{-23.89}$
NGC 6140	$19.79^{+0.06}_{-0.08}$	$22.74^{+4.66}_{-6.34}$	$1.1^{+0.1}_{-0.1}$	$19.03^{+0.40}_{-0.59}$	$43.45^{+8.51}_{-17.11}$
NGC 6384	$16.81^{+0.27}_{-0.15}$	$9.99^{+1.83}_{-1.43}$	$1.9^{+0.2}_{-0.1}$	$16.96^{+0.24}_{-0.20}$	$41.09^{+9.27}_{-12.77}$
NGC 6946	$16.09^{+0.22}_{-0.04}$	$12.24^{+1.47}_{-0.30}$	$2.2^{+0.2}_{-0.1}$	$16.95^{+0.10}_{-0.02}$	$127.18^{+21.50}_{-2.28}$
NGC 7727	$16.18^{+0.14}_{-0.24}$	$9.14^{+0.87}_{-1.56}$	$2.4^{+0.1}_{-0.2}$	$17.28^{+0.29}_{-0.39}$	$29.58^{+5.32}_{-8.90}$
NGC 7741	$18.88^{+0.04}_{-0.04}$	$8.43^{+0.36}_{-0.36}$	$0.6^{+0.1}_{-0.1}$	$18.38^{+0.05}_{-0.07}$	$38.76^{+1.93}_{-8.14}$

Table 3. Fitted bulge and disk parameters, not corrected for extinction or inclination

(e.g., Moriondo et al. 1998; Möllenhoff & Heidt 2001; Graham 2001). We note, however, that for spiral galaxies correlations between the disk parameters are severely affected by selection effects, most notably in the case of correlations involving μ_0 and h. Intrinsically large, high surface brightness galaxies are simply more likely to enter a magnitude or diameter limited sample than small, low surface brightness galaxies (Disney & Phillipps 1983; Allen & Shu 1979). These selection effects have to be taken into account to calculate proper distributions (de Jong & Lacey 2000; Blanton et al. 2001; Cross & Driver 2002). Furthermore, if bulge parameters are tightly correlated with disk parameters (like the $h/R_{e,B}$ ratio discussed below), then also the distribution of bulge parameters will be biased.

In Fig. 3 we show the reliable bulge and disk parameters as function of morphological T-type (from the RC3) and of best fitting n. As noted before (e.g., de Jong 1996b; Möllenhoff & Heidt 2001), the change from T-type 2 to 8 is strongly correlated with the change in bulge luminosity. The decrease in luminosity with increasing T-type is mainly

the result of bulge surface brightness changes helped a little bit by bulge shape changes, but is not due to bulge scale size changes.

Figure 3 also shows that the disk luminosities peak at about T-type 3-4, decreasing on average for earlier and later-types, driven mainly by surface brightness but partly by scale size, as observed before by de Jong (1996b) and Möllenhoff & Heidt (2001). The relative bulge to disk scale size ratio does not change much in this morphological type range as often observed before (e.g., de Jong 1996b; Courteau et al. 1996; Moriondo et al. 1998; Graham 2001; MacArthur et al. 2003). This implies that the change observed in B/T ratio as a function of morphological type, a change which is in itself not surprising as the B/T ratio is one of the criteria for defining morphological type, is mainly due to differences in the relative effective surface brightnesses of the bulge and the disk.

When now turning to the bulge and disk parameter correlations with n, we confirm previously known trends between n and bulge luminosity and surface brightness (e.g.,

Parameters	$r_{\rm s}$	Significance
Type $- B/T$	-0.75	0.047
Type $- \mu_{\rm e,B}$	0.46	0.169
Type $- M_B$	0.81	0.002
$n - M_B$	-0.54	0.083
Type $- n$	-0.53	0.090

Table 4. For a number of selected correlations, as discussed in the text (column 1), we list the Spearman rank-order correlation coefficient $r_{\rm s}$ (column 2) and significance (column 3), i.e., the probability that this relation occurs at random.

Andredakis et al 1995; Möllenhoff & Heidt 2001; Trujillo et al. 2002). These authors also report other correlations between n and, for instance, $R_{\rm e,B}$ and B/T, but we have too few data points to confirm such trends. Finally, there is a clear trend between morphological type and n, observed by most other authors, though not as strongly by MacArthur et al. (2003). We present correlation coefficients and significance indicators of some of the trends mentioned in Table 4. Almost all trends and parameter ranges are consistent with continuations of trends seen in a large sample of early-type galaxies studied by R. S. de Jong et al. (in preparation).

5   CONCLUDING REMARKS

In this paper, we present the first set of results of our study of the spiral arm and disk properties of a sample of 57 nearby, relatively face-on, spiral galaxies. We describe the sample selection and summarise some of the properties of the sample, and present a full set of NIR $K_{\rm s}$-band images of the sample galaxies. Those images have been obtained using the 4.2 m WHT and 2.3 m Bok telescopes, and with a minimum image size of 4.2 arcmin square cover most of the disk of all galaxies. We describe the data collection and reduction procedures, and show all resulting images.

We derive radial profiles to the light distribution of all sample galaxies, and perform 1D bulge/disk decomposition by fitting exponential disk and Sersic bulge profiles. The results of this exercise are shown, but due to the limited signal-to-noise ratio in our images we can fit both bulge and disk parameters in a reliable way for only 13 of our 57 galaxies, although either reliable bulge or disk parameters can be determined for more galaxies. Using the reliable bulge and disk parameters thus derived, we explore several correlations between those and galactic parameters such as morphological type. We confirm correlations between bulge and disk luminosities and morphological type, and between the Sersic parameter n and bulge luminosity and surface brightness, and morphological type.

In further papers in this series, we will publish the accompanying optical broad (B, I) and narrow-band (Hα) imaging, as well as analyses of disk scale lengths, and of properties of morphological entities such as bars and rings within the galaxies.

ACKNOWLEDGMENTS

REFERENCES

Aguerri J. A. L., Balcells M., Peletier R. F., 2001, A&A, 367, 428
Allen R. J., Shu F. H., 1979, ApJ, 227, 67
Andredakis Y. C., 1998, MNRAS, 295, 725
Andredakis Y. C., Peletier R. F., Balcells M., 1995, MNRAS, 275, 874
Blanton M. R., Dalcanton J., Eisenstein D., et al., 2001, AJ, 121, 2358
Block D. L., Puerari I., Knapen J. H., Elmegreen B. G., Buta R., Stedman S., Elmegreen D. M., 2001, A&A, 375, 761
Byun Y. I., Freeman K. C., 1995, ApJ, 448, 563
Courteau S., de Jong R. S., Broeils A. H., 1996, ApJ, 457, L73
Cross N., Driver S. P., 2002, MNRAS, 329, 579
de Jong R. S., 1996a, A&AS, 118, 557
de Jong R. S., 1996b, A&A, 313, 45
de Jong R. S., Lacey C., 2000, ApJ, 545, 781
de Vaucouleurs G., 1948, Annales d'Astrophysique, 11, 247
de Vaucouleurs, G., de Vaucouleurs, A., & Corwin, J. R. 1976, Second reference catalogue of bright galaxies, 1976, Austin: University of Texas Press (RC2)
de Vaucouleurs G., de Vaucouleurs A., Corwin J. R., Buta R. J., Paturel G., Fouque P., 1991, Third reference catalogue of Bright galaxies, 1991, New York : Springer-Verlag (RC3)
Disney M., Phillipps S., 1983, MNRAS, 205, 1253
Doyon R., Nadeau D., Vallee P., Starr B. M., Cuillandre J. C., Beuzit J., Beigbeder F., Brau-Nogue S., 1998, Proc. SPIE, 3354, 760
Elmegreen D. M., Elmegreen B. G., 1987, ApJ, 314, 3
Eskridge P. B., Frogel J. A., Pogge R. W., et al., 2000, AJ, 119, 536
Eskridge P. B., Frogel J. A., Pogge R. W., et al., 2002, ApJS, 143, 73
Graham A. W., 2001, AJ, 121, 820
Hawarden T. G., Leggett S. K., Letawsky M. B., Ballantyne D. R., Casali M. M., 2001, MNRAS, 325, 563
Hunt, L. K., Mannucci, F., Testi, L., Migliorini, S., Stanga, R. M., Baffa, C., Lisi, F., & Vanzi, L. 1998, AJ, 115, 2594
Jarrett T. H., Chester T., Cutri R., Schneider S. E., Huchra J. P., 2003, AJ, 125, 525
Jogee S., Shlosman I., Laine S., Englmaier P., Knapen J. H., Scoville N., Wilson C. D., 2002, ApJ, 575, 156
Knapen J. H., Shlosman I., Peletier R. F., 2000, ApJ, 529, 93
Knapen J. H., Stedman S., Bramich D. M., Folkes S., 2003, submitted to MNRAS (Paper II)
MacArthur L.A., Courteau S., Holtzman J.A., 2003, ApJ, 582, 689

McCarthy D. W., Ge J., Hinz J. L., Finn R. A., de Jong R. S., 2001, PASP, 113, 353

Möllenhoff C., Heidt J., 2001, A&A, 368, 16

Moriondo G., Baffa C., Casertano S., et al., 1999, A&AS, 137, 101

Mulchaey J., Regan M., 1997, ApJ, 482, L135

Packham C., Thompson K., Zurita, A., et al., 2003, MNRAS, submitted

Roche P. F., et al., 2002, Proc Spie 4841, Instrument Design and Performance for Optical/IR Ground-Based Telescopes, eds. M. Iye and A. F. M. Moorwood

Sandage A., Bedke J., 1994, Washington, DC: Carnegie Institution of Washington with The Flintridge Foundation

Schlegel D. J., Finkbeiner D. P., Davis M., 1998, ApJ, 500, 525

Sersic J. L., 1968, Cordoba, Argentina: Observatorio Astronomico

Seigar M. S., James P. A., 1998a, MNRAS, 299, 672

Seigar M. S., James P. A., 1998b, MNRAS, 299, 685

Sellwood J.A., Wilkinson A., 1993, Rep. Prog. Phys., 56, 173

Simard L., Willmer C. N. A., Vogt N. P., et al., 2002, ApJS, 142, 1

Skrutskie M. F., et al., 1997, in The Impact of Large Scale Near-IR Sky Surveys, ed. F. Garzon et al. (Dordrecht: Kluwer), 187

Stedman S., Knapen J. H., 2001, Ap&SS, 276, 517

Tran, K.-V., Simard, L., Illingworth, Franx, M., 2003, ApJ, in press (astro-ph/0302292)

Trujillo I., Asensio Ramos A., Rubiño-Martín J. A., Graham A. W., Aguerri J. A. L., Cepa J., Gutiérrez C. M., 2002, MN-RAS, 333, 510

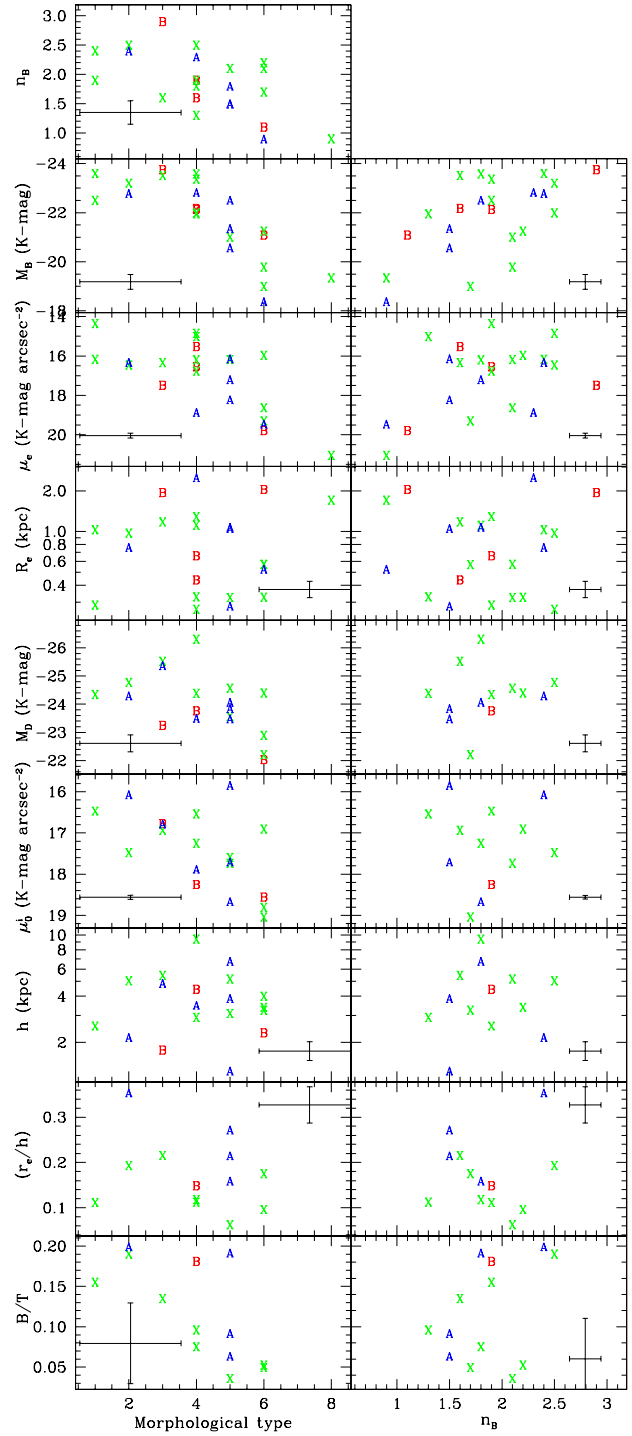Tully, R. B. 1988, Cambridge and New York, Cambridge University Press

Figure 3. Various disk and bulge parameters as function of morphological T-type and Sersic n bulge shape parameter. Non-barred galaxies are indicated by A, barred galaxies by B and X are used for intermediate types. The errorbars indicate the median errors for the plotted galaxies.
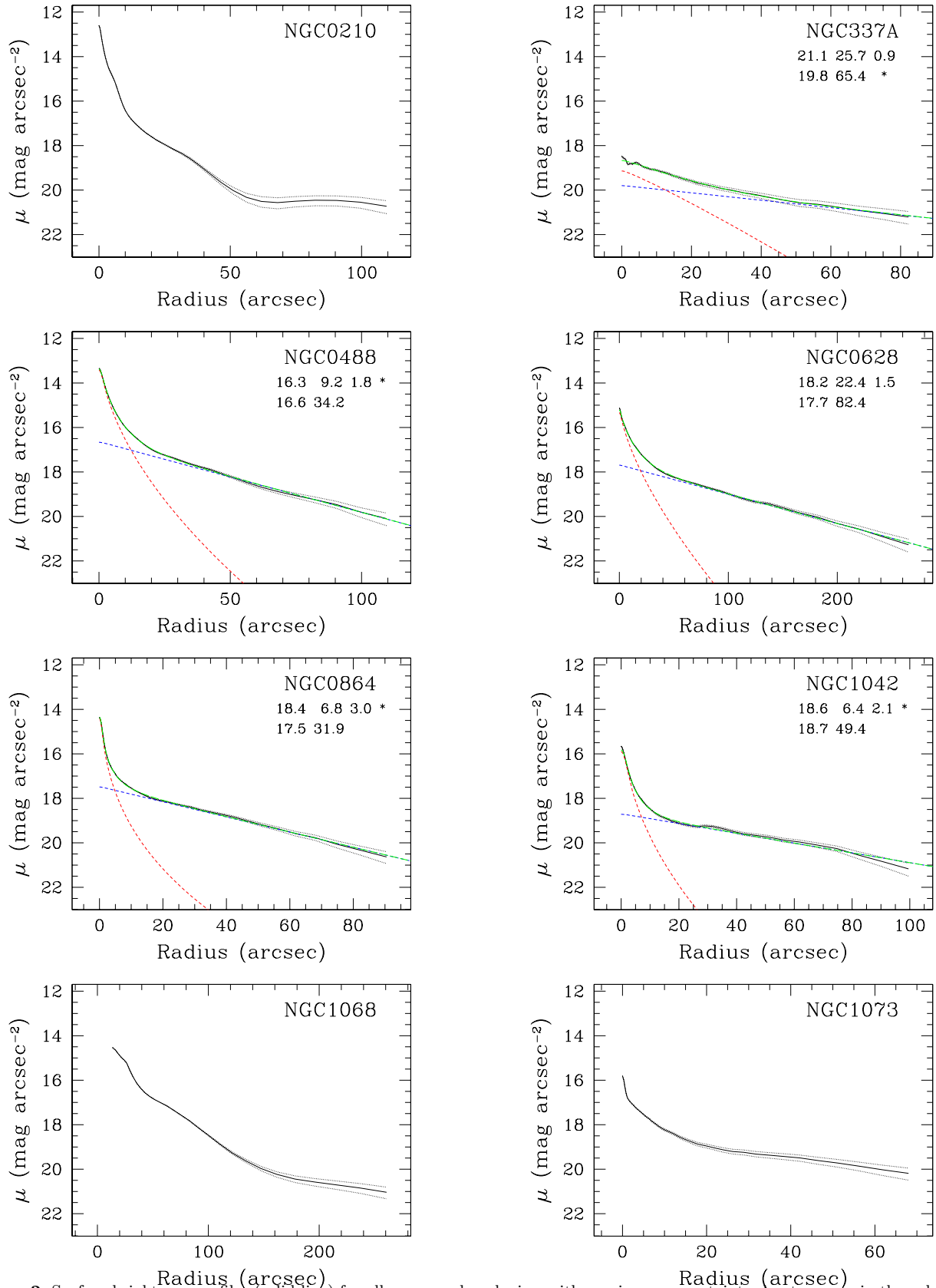
Figure 2. Surface brightness profiles (solid line) for all our sample galaxies, with maximum uncertainty due to errors in the subtraction of sky background indicated by the dotted lines. Bulge/disk decompositions are only plotted if at least one component had errors less than 30%. Bulge and disk fits are indicated by short-dashed lines, the sum of the fitted components by a long-dashed line, and the fit parameters are listed below the NGC number. The bulge parameters: $\mu_{e,B}$ (in K-mag arcsec^{-2}), $R_{e,B}$ (in arcsec) and n, respectively, are given on the top line, the disk parameters: μ_0 (in K-mag arcsec^{-2}) and h (in arcsec) on the bottom line. All components with parameter uncertainties larger than 30% due to sky background subtraction errors have been marked by a star.   © 2003 RAS, MNRAS **000**, 1–9
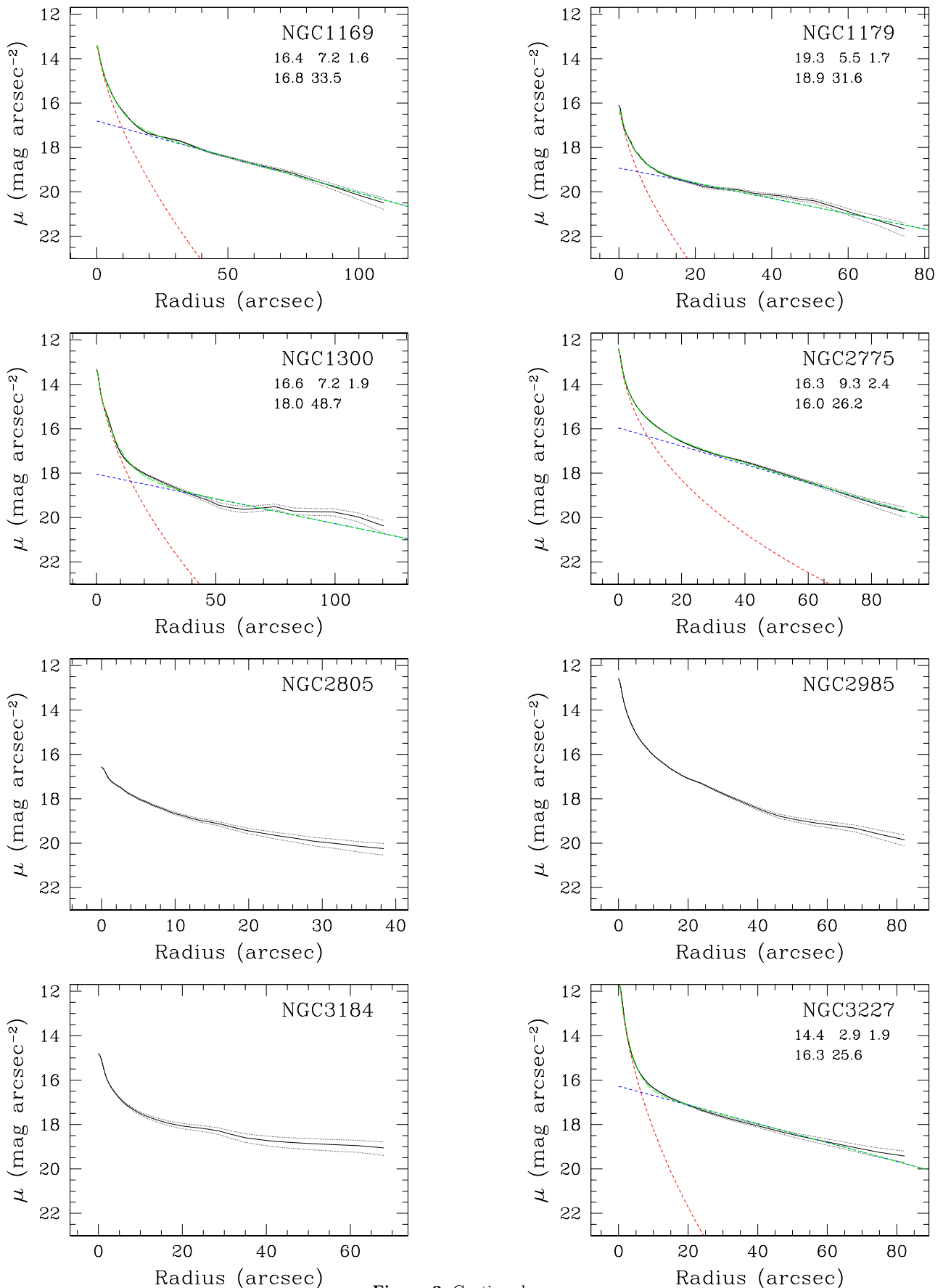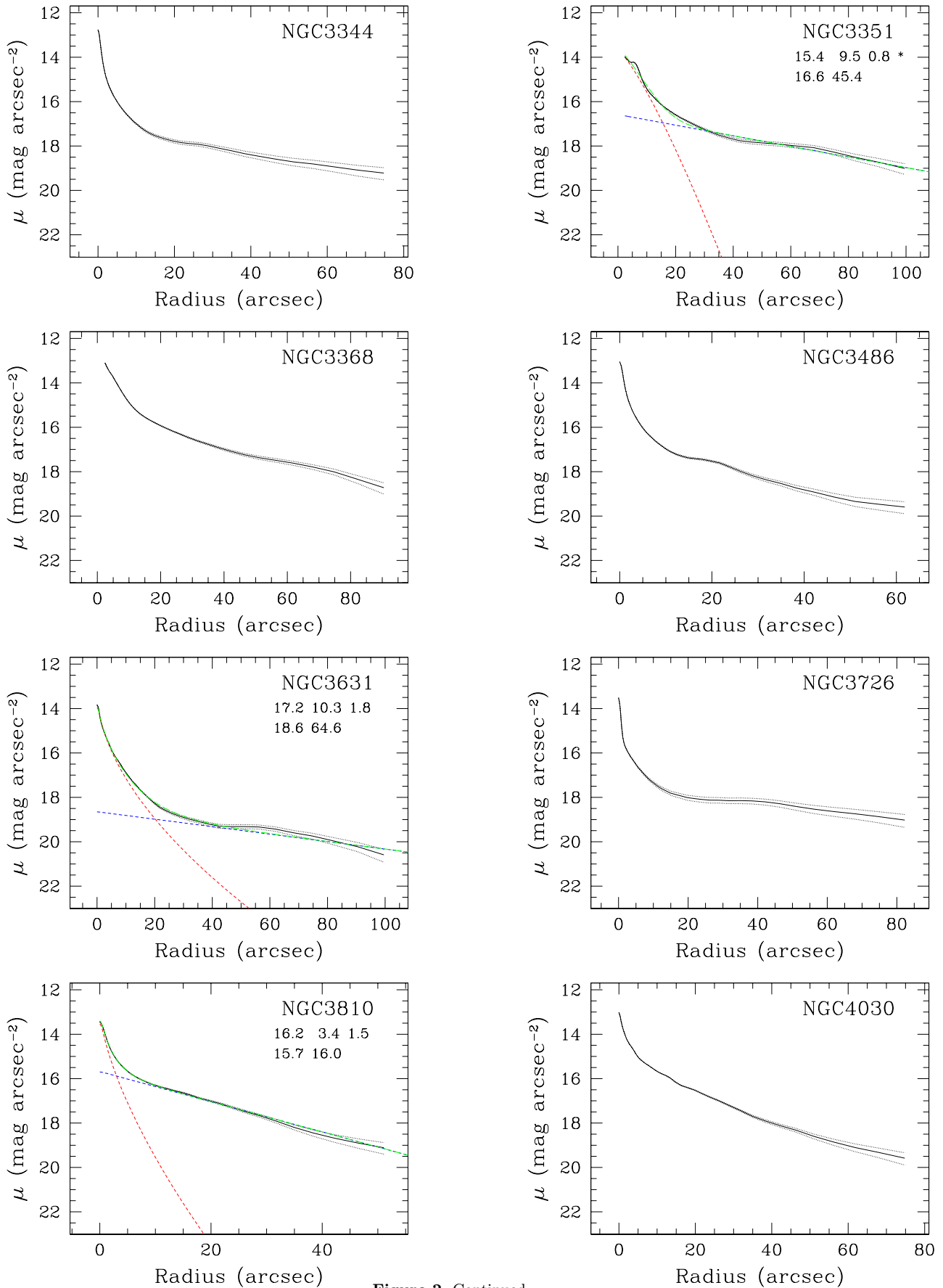
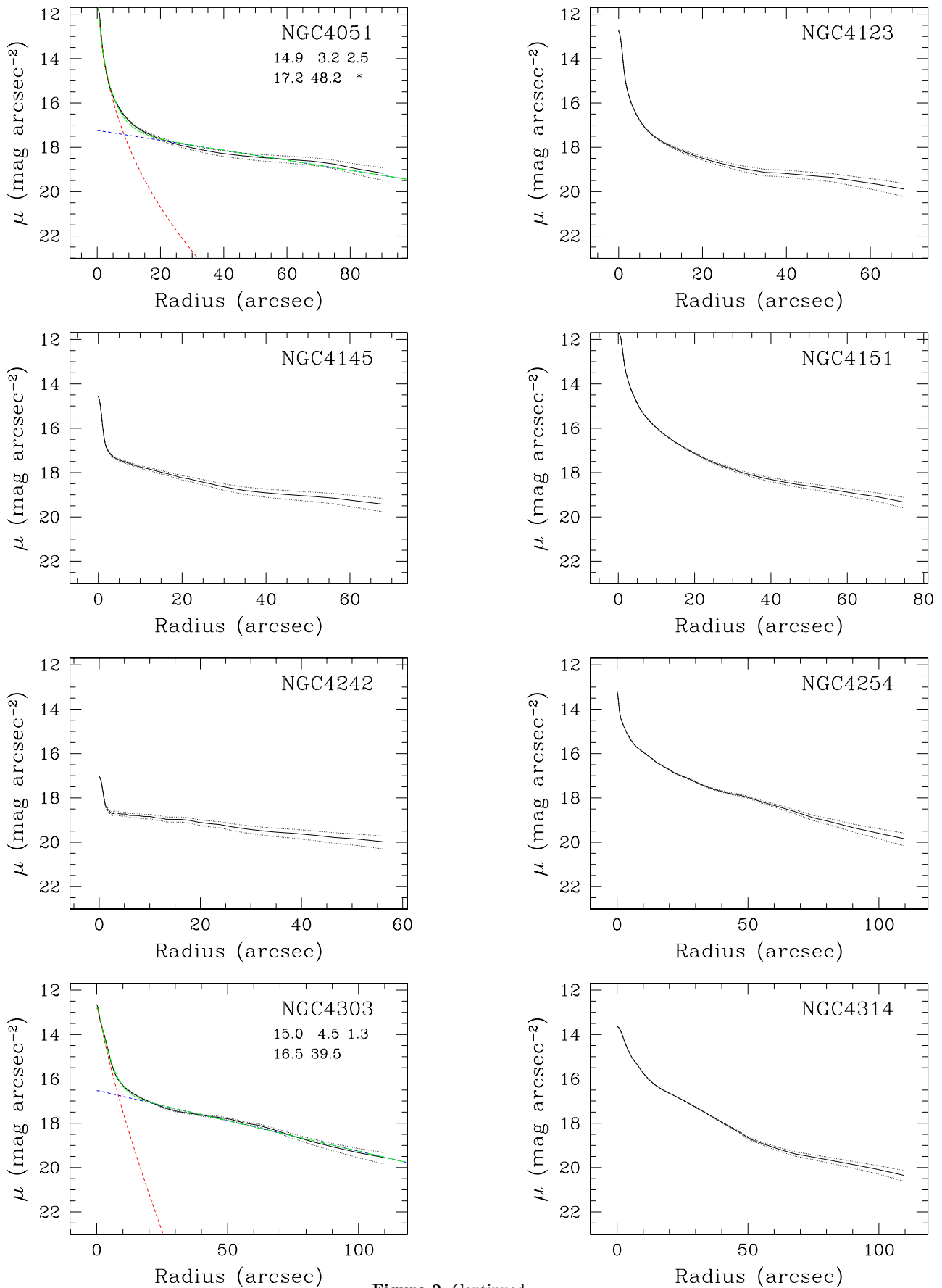**Figure 2.** Continued.

Figure 2. Continued.

NGC4051

14.9 3.2 2.5
17.2 48.2 *

NGC4123

NGC4145

NGC4151

NGC4242

NGC4254
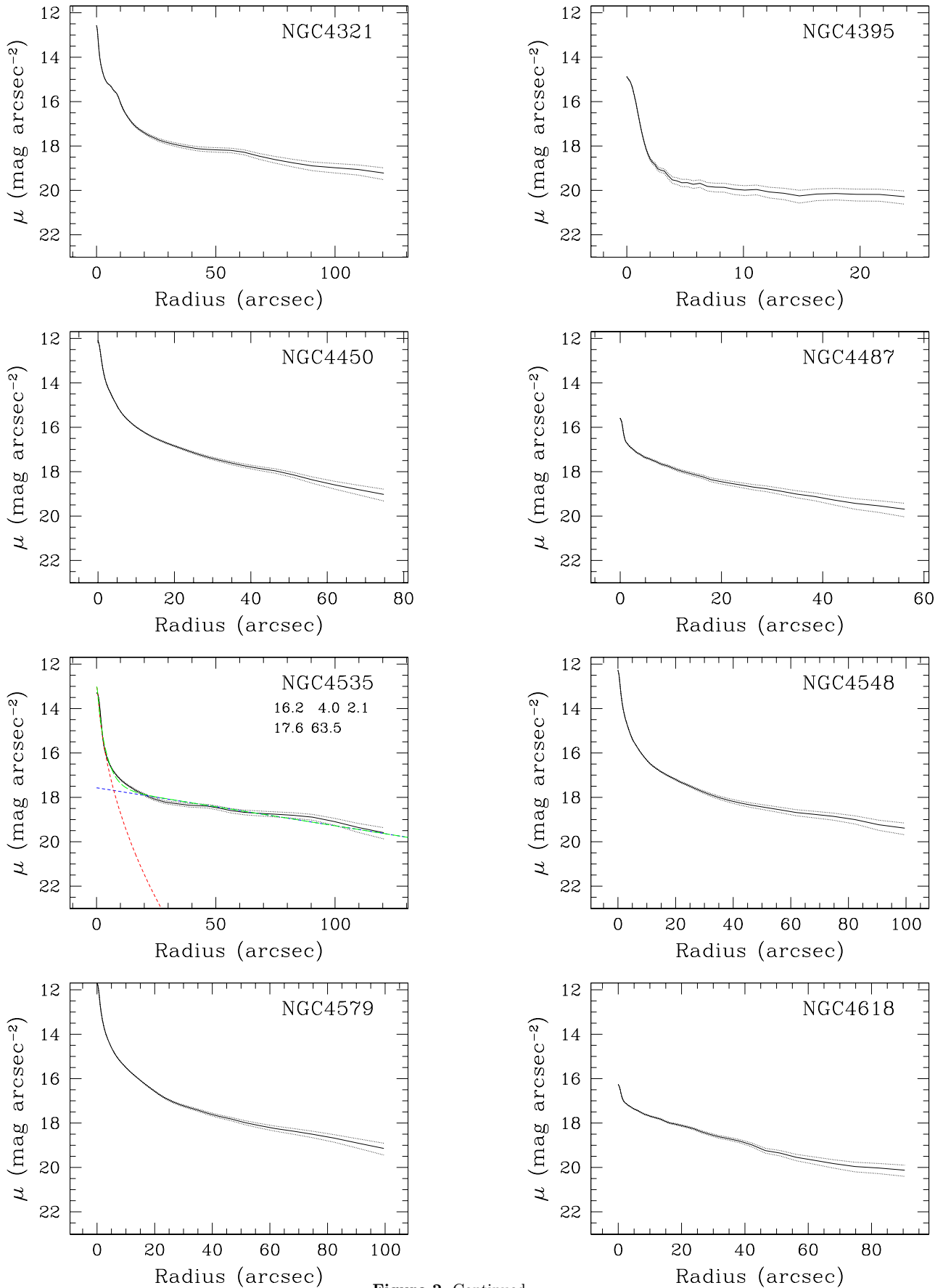
NGC4303

15.0 4.5 1.3
16.5 39.5

NGC4314
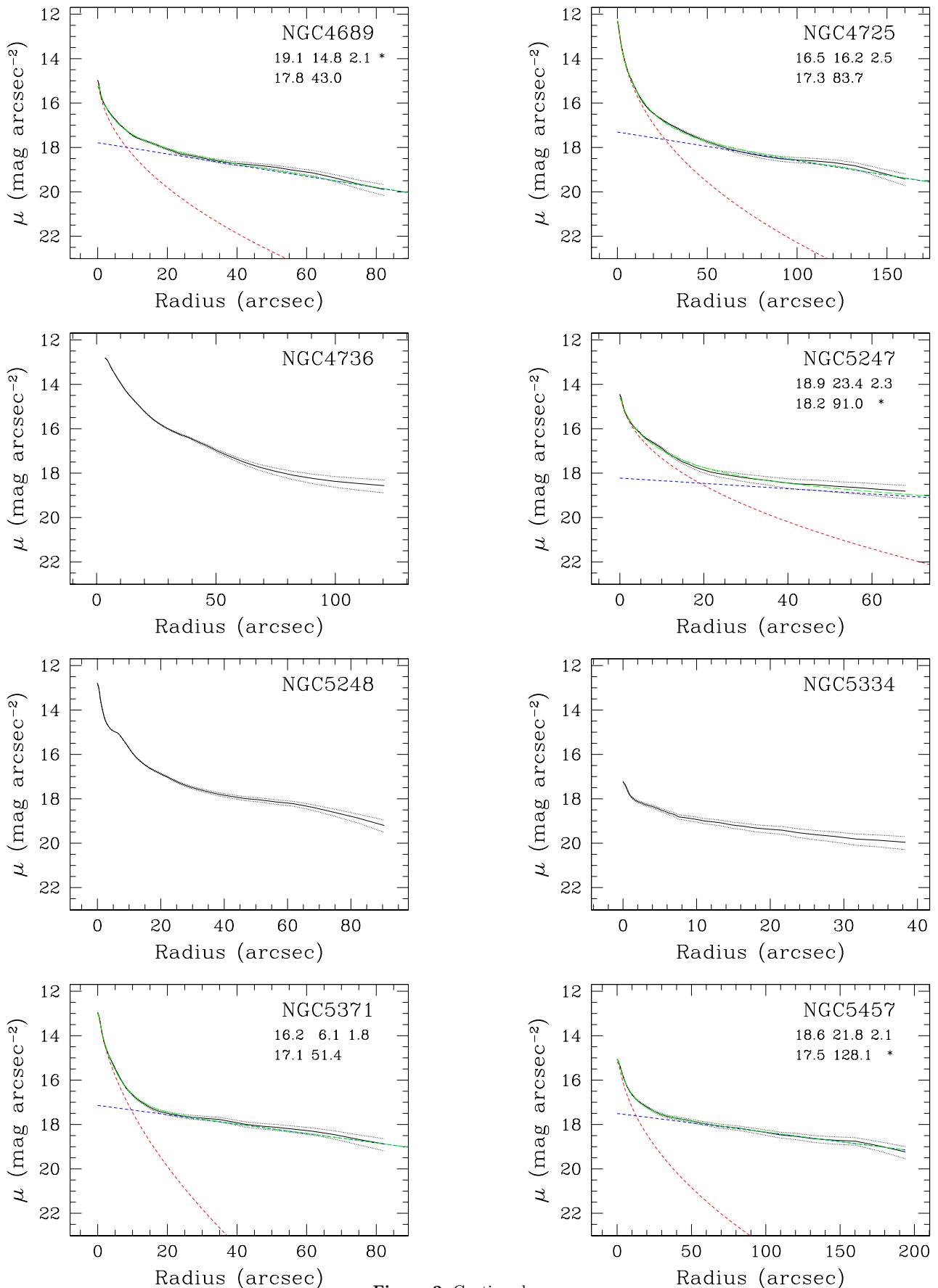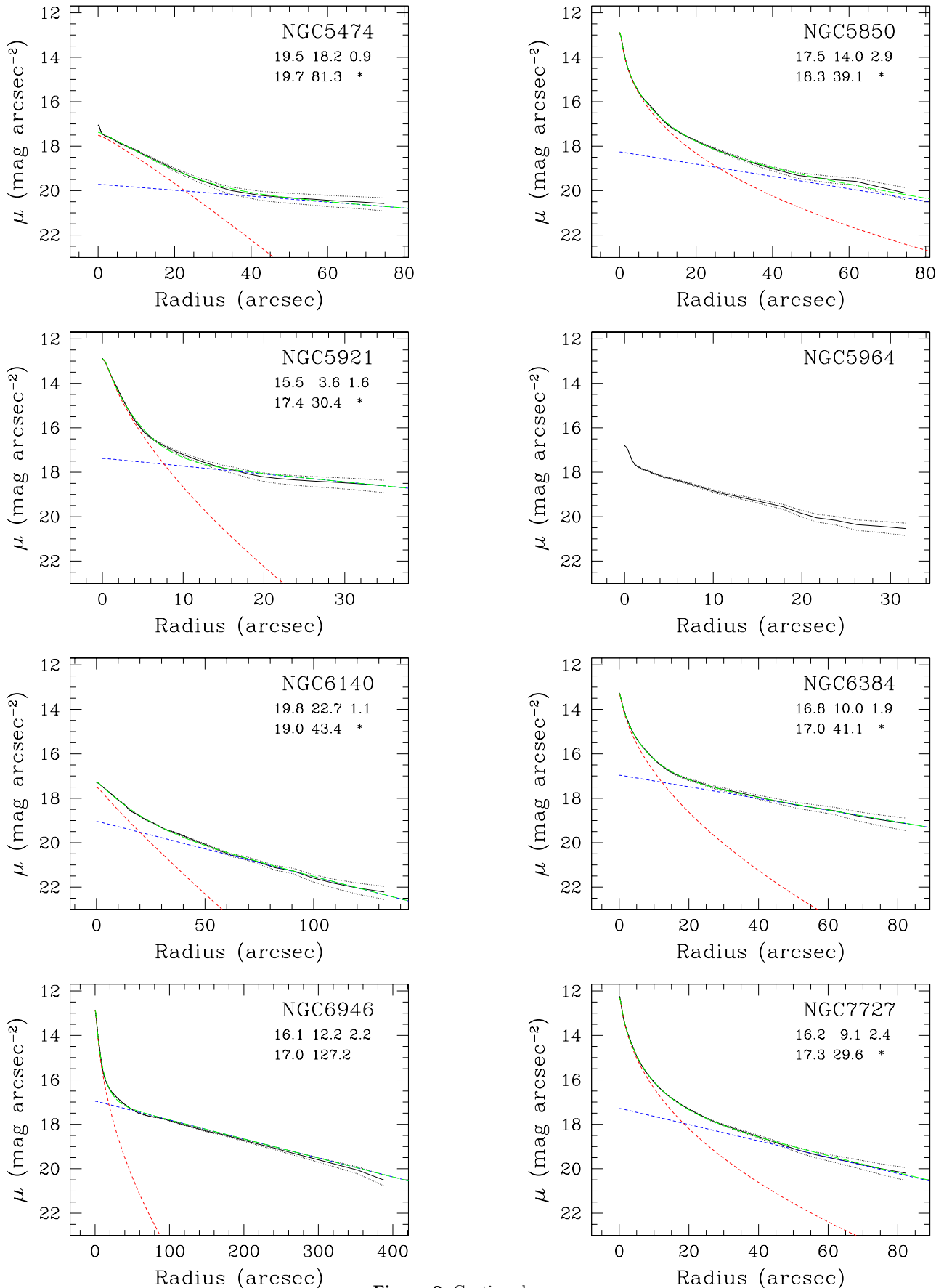
Figure 2. Continued.

Figure 2. Continued.

Figure 2. Continued.

Figure 2. Continued.

This figure "panel1.jpg" is available in "jpg" format from:

http://arxiv.org/ps/astro-ph/0303613v2

This figure "panel2.jpg" is available in "jpg" format from:

http://arxiv.org/ps/astro-ph/0303613v2

This figure "panel3.jpg" is available in "jpg" format from:

http://arxiv.org/ps/astro-ph/0303613v2